Justin Thomas[1]
GRASP Lab,
Department of Mechanical Engineering
and Applied Mechanics,
University of Pennsylvania,
Philadelphia, PA 19104
e-mail: jut@seas.upenn.edu

Morgan Pope
Department of Mechanical Engineering,
Stanford University,
Stanford, CA 94305
e-mail: mpope@stanford.edu

Giuseppe Loianno
GRASP Lab,
Department of Mechanical Engineering
and Applied Mechanics,
University of Pennsylvania,
Philadelphia, PA 19104
e-mail: loiannog@seas.upenn.edu

Elliot W. Hawkes
Department of Mechanical Engineering,
Stanford University,
Stanford, CA 94305
e-mail: ewhawkes@stanford.edu

Matthew A. Estrada
Department of Mechanical Engineering,
Stanford University,
Stanford, CA 94305
e-mail: estrada1@stanford.edu

Hao Jiang
Department of Mechanical Engineering,
Stanford University,
Stanford, CA 94305
e-mail: jianghao@stanford.edu

Mark R. Cutkosky
Department of Mechanical Engineering,
Stanford University,
Stanford, CA 94305
e-mail: cutkosky@stanford.edu

Vijay Kumar
GRASP Lab
Department of Mechanical Engineering
and Applied Mechanics,
University of Pennsylvania
Philadelphia, PA 19104
e-mail: kumar@seas.upenn.edu

Aggressive Flight With Quadrotors for Perching on Inclined Surfaces

Micro-aerial vehicles (MAVs) face limited flight times, which adversely impacts their efficacy for scenarios such as first response and disaster recovery, where it might be useful to deploy persistent radio relays and quadrotors for monitoring or sampling. Thus, it is important to enable micro-aerial vehicles to land and perch on different surfaces to save energy by cutting power to motors. We are motivated to use a downward-facing gripper for perching, as opposed to a side-mounted gripper, since it could also be used to carry payloads. In this paper, we predict and verify the performance of a custom gripper designed for perching on smooth surfaces. We also present control and planning algorithms, enabling an underactuated quadrotor with a downward-facing gripper to perch on inclined surfaces while satisfying constraints on actuation and sensing. Experimental results demonstrate the proposed techniques through successful perching on a glass surface at various inclinations, including vertical. [DOI: 10.1115/1.4032250]

Introduction

MAVs suffer from limited energy-density storage, which significantly restricts their mission time [1]. Many tasks, however, do not require the robot to be in motion. In fact, some tasks do not even require the robot to be airborne. For example, a robot may be given the objective to monitor a crime scene until police arrive or to monitor the gas levels of a nearby gas leak. In such cases, the vehicle could not only be stationary but also perch and turn off its motors to preserve energy for the next task. Perching could also be useful for tasks which require the robot to maintain a static position, act as a radio relay in disaster zones, or to suspend operation when not needed or during a period of unfavorable weather. Thus, the ability to perch is critical to sustained operations in a wide range of missions.

Fixed wing vehicles have been shown to perch on vertical walls using penetration-based grasping [2–4] and on cables such as power lines [5,6]. However, the challenges of object detection and

[1]Corresponding author.

Manuscript received September 21, 2015; final manuscript received December 3, 2015; published online May 4, 2016. Assoc. Editor: James Schmiedeler.

recognition as well as relative pose estimation using onboard sensors and computation in real-time, real-world, scenarios would make such approaches very difficult in practice for fast-moving, microsized fixed-wing aircraft.

In comparison to fixed wing vehicles, quadrotors can carry larger payloads for their size (i.e., more processing power, more sensors, and greater payload per footprint) and can provide both slow and fast, agile movements, which makes them useful in many scenarios. Their flight time is more restricted, however, which makes the motivation for perching even stronger. Passive gripping mechanisms were developed for perching in Refs. [7–9], but the mechanisms consume a large fraction of the available payload and are restricted to objects that are narrow enough for the gripper to wrap around. Similarly, Ref. [10] presents a gripper that requires cylindrical objects and would restrict the set of possible perch locations based on the size of the gripper. Dry adhesives are used to adhere to flat surfaces in Ref. [11], but a planning or control strategy for the robot to achieve perching is not presented. The authors in Refs. [12] and [13] use dry adhesives while Ref. [14] uses suction for perching. However, in these cases, the gripper is placed on the side of the robot, requiring extra compensation for the added moment and rendering the gripper unlikely to be useful for tasks such as transportation of objects. An opposed-grip dry adhesive is used in Ref. [15] to increase the capable load, but a launcher is used to simulate a perching maneuver.

In a related prior work, a bioinspired trajectory generation method (tau theory) is used for perching [16]. However, the dynamics and underactuation of the robot are not considered, and only kinematic simulations are provided. The authors of Refs. [17] and [18] present perching on vertical surfaces, but the gripper uses a hook and loop fastener, VELCRO®, for adhesion, which is not desirable for real-world scenarios since it would require preestablished perch locations and would make release from the perch location challenging. Furthermore, they rely on switching between linear controllers as well as iterative learning for successful perching. Their work is extended in Ref. [19] where time constants for attitude commands are incorporated, but the system still uses a state machine to toggle between a trajectory and attitude controller, which ultimately requires an iterative learning approach. All sensing and processing is conducted onboard the robot in Ref. [20], but the perching is achieved using a hook and loop fastener.

In our previous work, a robot was able to grasp objects while the robot was in motion, and the extension to perching would be straightforward [21]. However, the gripper had a large inertia relative to that of the robot, which impacted the dynamics of the overall system and motivated its consideration when planning aggressive trajectories for grasping. Additionally, possible perch locations were limited to horizontal flat surfaces or sufficiently small cylinders. Since an aerial robot would most often be observing things below, it is desirable to avoid perching on level surfaces since they would interfere with downward observations. Further, in cases such as urban environments, the best available surfaces may be vertical windows, walls, or inclined roof tops.

In this article, which further develops [22], we present a method that incorporates both a downward-facing, real-world gripping mechanism as well as a planning and control strategy for quadrotors to achieve the necessary conditions for perching on smooth, inclined surfaces (see Fig. 1). A passively actuated, downward-facing, dry-adhesive gripper is presented and used to adhere to such surfaces, and its requirements for successful perching on vertical surfaces are defined. The downward-facing gripper motivates a strategic approach for trajectory planning since the system is underactuated such that the orientation and the position of the robot cannot be independently controlled. Thus, we present a suitable method for trajectory generation, which considers actuator and sensor constraints to ensure that the planned trajectories are not only dynamically feasible but also realizable on the physical platform. Further, we ensure that the robot gripper contacts the perching surface with an approach orientation and velocity within a required *landing envelope*. Finally, we show experiments using a quadrotor equipped with the proposed gripper.

The key contributions of this paper are threefold: (1) We model and characterize a passively actuated, opposed-grip, dry adhesive gripper in terms of the conditions necessary for successful MAV perching. (2) We present a method for control and planning to ensure that the robot's perch will fall within the landing envelope. (3) We experimentally demonstrate the effectiveness of the planning strategy, the controller, and the gripper.

The rest of the paper is organized as follows: first, we provide an overview of the design of the gripper, propose a model for the landing envelope, and explore the landing envelope of the gripper experimentally. Following the gripper design, the dynamics and the controller for the robot are presented. Then, a method for planning physically realizable trajectories considering actuator and sensor constraints is developed. Finally, experimental results are demonstrated, and we conclude the paper, offering paths for continued development.

A Gecko Inspired Gripper

We used a gripper influenced by the opposed-grip dry adhesive design described in Ref. [23]. The device is "gecko-inspired" because of the dry adhesive used—a nontacky silicone rubber with microscopic surface texturing that enables it to controllably switch between adhesive and nonadhesive states through the application of a shear force. This is inspired by the way a gecko uses microstructures on its toes to adhere to surfaces. On dry, smooth surfaces, the adhesive can achieve up to 10 kPa in normal adhesive force [23]; however, surfaces rougher than glass or

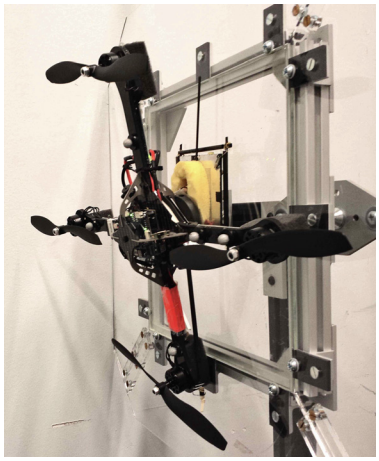

Fig. 1 A quadrotor perched on a vertical glass surface

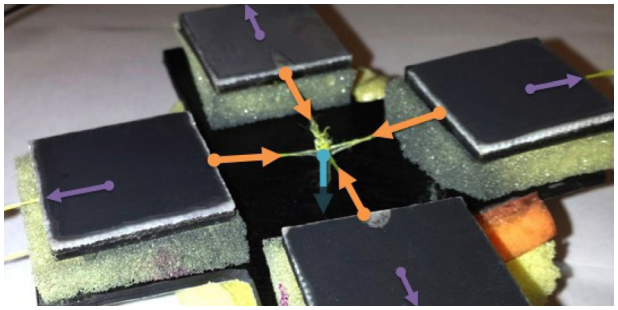

Fig. 2 A view of the underside of the gripper. Initially, the pads are held in place by slight tension between the outer tendons (indicated by outwards-pointing arrows) and the inner tendons (indicated by the inwards-pointing arrows). Then, upon the collapse of the truss mechanism, each pad is placed in shear by pulling the pad toward the center of the gripper using the tension string (downward, partially occluded arrow).

acrylic will show some degradation in performance. Further, the material is stable over a wide range of temperatures, making it a viable solution for outdoor scenarios. By placing two adhesive tiles in opposition with an internal shear force, the tiles can achieve adhesion independent of surface orientation. The adhesive is lightweight (the 25 cm^2 of adhesive tile is only 12 g and can support a 580 g robot) and enables perching on smooth surfaces. The total mass of the gripping mechanism and suspension, including the dry-adhesive tiles, is 60 g.

To provide an adequate safety factor for the perching maneuver, two pairs of adhesive tiles were used. These are arranged in a cross shape, as illustrated in Fig. 2. Both pairs are anchored to the same frame, a circle made out of a bent carbon fiber rod. This provides a consistent preload for both sets and keeps them in the same plane during the approach to the wall. Because of the tight tolerances maintained in this configuration, it was found to be unnecessary to use a differential mechanism (e.g., pulleys or links as in Ref. [24]) to ensure even force distribution. Instead, both pairs are loaded through a single tendon attached at the center of the mechanism. In its final realization, the weaker of the two pairs averaged a failure load of 7.53 N, and the combined mechanism averaged a failure load of 14.2 N, which is 94% of the theoretical limit (calculated by doubling the limit of the weaker pads).

When perching with a quadrotor, aerodynamic surface effects tend to repel the vehicle from the target surface, and stray breezes can deflect a slow-moving vehicle just prior to impact. Both of these considerations motivate a relatively high incoming velocity so that the duration and impact of these effects is minimal. However, impact at such velocities results in high demands on the loading rate of any chosen gripper. In our case, the adhesives must be loaded within a 10 ms window when they are in active compression against the wall, or else premature failure can occur. As described in Ref. [23], this can be addressed by using a collapsing truss mechanism to guarantee an effective loading cycle, as illustrated in Fig. 3. The truss compensates for high incoming velocities and can passively reset itself after a successful perch. A failed perch, however, requires recovery from the failure and also a manual reset of the truss mechanism. Future work will build upon the recovery strategies outlined in Refs. [25] and [26], and the mechanism will be further developed to automate a reset.

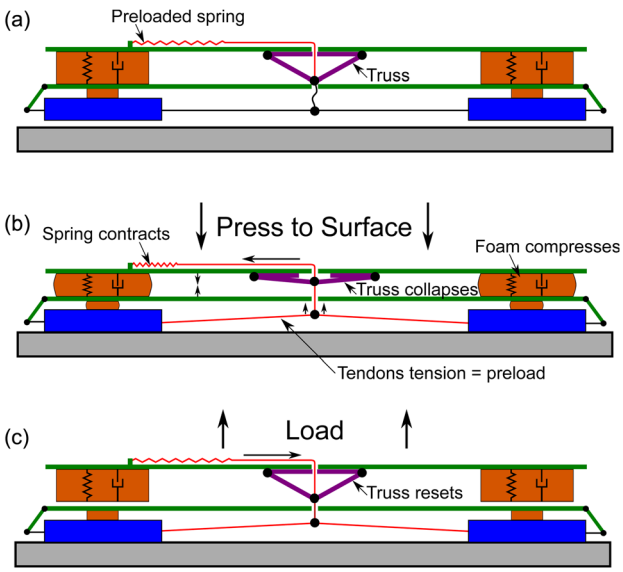

Fig. 3 A cross section view of the gripper (reproduced from Ref. [23]). The bistable truss mechanism is used to engage the directional adhesive pads upon contact with the surface. (*a*) Initially, a preloaded spring is tensioned low enough that the truss does not collapse. (*b*) Upon impact, the truss collapses (the magnets holding the one side together separate) and the tension in the spring is transmitted via tendons to the gripping pads to create shear. Since the mechanism is still in compression, the shear force results in an appropriate loading cycle for high speed engagement. (*c*) When the robot creates tension in the tendon, whether from the rebound or from static hanging, the truss mechanism resets, and the tension remains transmitted to the pads since the entire mechanism is being pulled away.

Landing Envelope Modeling and Verification. The set of impact conditions which lead to success—the *landing envelope* for a perching vehicle—have previously been characterized for dry adhesive grippers in Ref. [15] using a numerical simulation and in Ref. [23] as an empirical result. Out of the range of possible state variables, two have proved crucial to understanding the performance of a given gripper on a specific robot—the velocity of the robot in the direction normal to the target surface (normal velocity) and the velocity of the robot parallel to the target surface (tangential velocity). We follow the approach used in Ref. [27] to model a ballistic perching and climbing robot, and we extend it to the case of an incoming quadrotor to predict one boundary of the landing envelope. Next, we use empirical results and observations to complete the description of the safe region. Then, we briefly discuss our current understanding of the limits on other state variables, and formalize the landing envelope.

Bounds on Rebound Spring Energy Storage. The gripper is attached to the quadrotor by a compliant element referred to as the rebound spring, which is designed to keep the forces transmitted to the gripper below the adhesive limit of the pads until it reaches the hard stop at the end of its travel. In Ref. [27], it was shown that the potential energy stored in the rebound spring before hitting the upper limit was an effective predictor of the upper bound of incoming velocity. Note that this requires consideration of the coefficient of restitution in the direction normal to the wall to predict the rebound velocity after energy is dissipated in the suspension. The addition of foam between the mechanism and the quadrotor significantly increases damping in the normal direction. Foam is also placed underneath each rotor to soften their impact with the wall and help orient the robot consistently after perching, which also contributes to normal damping. Damping in the direction tangential to the surface is small because the adhesive pads generally adhere to the surface without translating, thus preventing the accumulation of frictional work along that boundary. With this in mind, we specify a boundary based on the energy storage of the rebound spring by integrating the spring force $F(l)$ over the spring length l. By defining the coefficient of restitution c in the normal direction, a limit on incoming velocity $\dot{\mathbf{x}} \in \mathbb{R}^3$ can be stated as

$$\frac{1}{2}m\left((\dot{\mathbf{x}}\cdot\mathbf{p}_1)^2+(\dot{\mathbf{x}}\cdot\mathbf{p}_2)^2+(c\,\dot{\mathbf{x}}\cdot\mathbf{p}_3)^2\right) < \int_{l_{\min}}^{l_{\max}} F(l)dl \qquad (1)$$

where m is the mass of the vehicle, $\mathbf{p}_3$ is a unit vector pointing into to the plane, and $\mathbf{p}_1$ and $\mathbf{p}_2$ are orthogonal unit vectors in the plane.

By launching the quadrotor against the wall with the dry adhesive surface covered, we were able to measure the coefficient of restitution in the normal direction for the current system. The average of six trials is resulted in a value of 0.30. The rebound spring applies an average force of 7.2 N over 5.0 cm of travel, resulting in 0.36 J of stored energy, which is equivalent to having an initial rebound velocity of 1.1 m/s. This limit on the energy storage results in the lower dashed curve in Fig. 5.

Maximum Upward Velocity and Pad Alignment. When rotating to present the pads to a vertical surface, the quadrotor loses the ability to counteract gravity and begins to accelerate downward. Thus, in order to avoid large negative tangential velocities at impact, the robot must acquire sufficient upward velocity in the

first part of the approach maneuver. Note that we use the term *tangential velocity* to mean the velocity along the plane which, in the vertical surface case, would be a velocity in the vertical direction. A desired positive (i.e., upward) tangential velocity requires a greater initial vertical velocity (and also, a longer vertical acceleration), which increases the minimum height requirement for the entire maneuver. In practice, this means that target velocities that are less than or equal to zero are easier to achieve, especially when the vertical distance for perching is constrained.

With this in mind, the gripper is designed to function best when impacting the wall with negative (i.e., downward) tangential velocity. As illustrated in Fig. 4, the angle at which the pads initially contact the surface must be matched to the expected tangential velocity at the time of impact. If the leading tile impacts the wall first, friction with the wall pushes the tiles closer together, creating slack in the tendon connecting them and leading to a final loading angle which is too steep to realize the full adhesive capability of the material. If the trailing tile impacts first, the tension in the connecting tendon maintains an appropriate distance between the tiles and still ensures proper loading. Therefore, the joint between the quadrotor and the gripper is designed so that the upper adhesive tile contacts the wall first. Further, the maneuver is specified so that the quadrotor impacts the wall with the upper arm inclined slightly toward the surface, which also has the benefit of requiring a smaller angle of rotation and less time to rotate. This impact orientation, however, creates problems for perch attempts with positive tangential velocity, motivating an upper limit of 0 m/s, which is represented as a horizontal dashed line in Fig. 5. Our future work will consider this effect in other directions, since wind gusts could induce velocity errors in the lateral or tangential directions and could lead to nonideal loading of the adhesive tiles unless the angle of impact is adjusted accordingly.

Minimum Normal Velocity. A lower bound in the normal direction is a result of velocities which are too slow to effectively align and engage the pads in compression. A statistical analysis of the failures between the energy storage limit curve and the tangential velocity limit provides an estimated lower boundary of 0.8 m/s. This limit appears as the vertical dashed line in Fig. 5. The adhesives themselves require very little preload force; thus, it is conceivable that a design optimized for low speeds could significantly reduce this limit and will be explored in future work.

Formalization of the Landing Envelope. The orientation of the robot, $R \in \mathrm{SO}(3)$, should be such that the gripper is angled slightly toward the target plane (see Fig. 4) and with minimal angular velocity, $\Omega \in \mathbb{R}^3$. Future work will explore the full effect of orientation, which currently has been controlled to be parallel to the plane in most tests. The lateral velocity along the surface has also been controlled to be small, but should have an effect similar to increased velocity in the tangential direction. Let the orientation of the plane be defined using the following right-handed basis such that $\mathbf{p}_3$ is a unit vector that is normal and pointed into the surface, $\mathbf{p}_2$ is a unit vector that is horizontal in the world and lays on the surface, and $\mathbf{p}_1 = \mathbf{p}_2 \times \mathbf{p}_3$, which is parallel to the surface and pointing upward in the world (angle depends on the inclination). Then, we can formalize the landing envelope in terms of the robot's position $\mathbf{x}$, velocity $\dot{\mathbf{x}}$, orientation R, and angular velocity Ω (see Eq. (2)).

$$\left\{ \mathbf{x}, \dot{\mathbf{x}}, R, \Omega \;\middle|\; \begin{array}{l} \mathbf{x} = \text{robot perch location} \\ \dot{\mathbf{x}} \cdot \mathbf{p}_1 < 0 \text{ m/s} \\ \dot{\mathbf{x}} \cdot \mathbf{p}_2 = 0 \text{ m/s} \\ \dot{\mathbf{x}} \cdot \mathbf{p}_3 > 0.8 \text{ m/s} \\ \frac{1}{2} m \left((\dot{\mathbf{x}} \cdot \mathbf{p}_1)^2 + (0.3 \dot{\mathbf{x}} \cdot \mathbf{p}_3)^2 \right) < 0.36 \text{ J} \\ R \text{ s.t. top slightly angled towards plane} \\ \Omega = \mathbf{0} \text{ rad/s} \end{array} \right\} \tag{2}$$

Verification of Normal and Tangential Velocity Bounds. The predicted bounds for the landing envelope were verified by launching the unpowered quadrotor against a vertical surface, recording its motion using a high-speed camera, and plotting the successes and failures as green dots and red squares, respectively, in Fig. 5. When flying autonomous, powered perches, the maneuvers targeted velocities near the middle of the safe region. Successes from flown perches are represented by diamonds in Fig. 5.

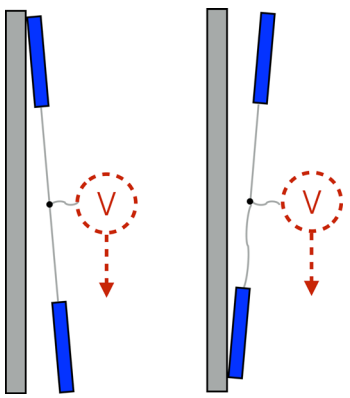

Fig. 4 Qualitative illustration of a failure mode due to an inappropriate matching of tangential velocity and adhesive tile orientation at impact. In (*a*), the trailing tile impacts first, maintaining tension between the two tiles and preserving a consistent final tile spacing and an appropriate final loading angle of the tendon. In (*b*), the leading tile impacts first, causing the connecting tendon to go slack and allowing the tiles to settle on the wall closer to each other than intended. This results in inconsistent and nonoptimal loading on rebound, increasing the chance of failure.

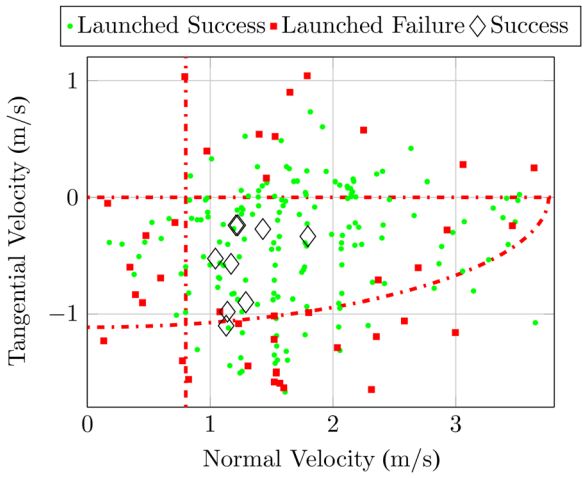

Fig. 5 The perching envelope of the quadrotor based on impact velocities relative to a vertical surface. Successful unpowered (i.e., launched) perches are shown as dots, and unpowered failures are shown as squares. Diamonds indicate successes for trials while the quadrotor was flying under its own power. Predicted boundaries are shown as dashed-dotted lines. The parabolic boundary is determined by calculating the kinetic energy after rebound relative to the maximum energy storage in the rebound spring. The left boundary is estimated based on the recorded low-speed failures, and the top boundary is based on the improper engagement failure observed for upward (positive) impact velocities. One can observe that a reasonable target normal velocity is 1.4 m/s with a tangential velocity of 0.4 m/s in the downward direction.

In flight, the planning and control strategies described in the rest of this paper are able to achieve landing conditions which meet these requirements, resulting in the successful perches (plotted as diamonds in Fig. 5).

In future work, the method described here for estimating the effective landing envelope should be easily extended to different quadrotors, simply by adjusting the mass, coefficient of restitution, and spring energy used in Eq. (1).

Dynamics and Control

In this work, the robot used is a quadrotor, which is a multirotor vehicle consisting of four rotors with parallel axes of rotation as displayed in Fig. 6. The rest of this section will present the dynamics of the system followed by a control law.

Preliminaries and Dynamics. The speed of the rotors, ω_i, can be mapped uniquely to the control inputs of the system using the following invertible transformation:

$$\begin{bmatrix} f \\ M_1 \\ M_2 \\ M_3 \end{bmatrix} = \begin{bmatrix} k_f & k_f & k_f & k_f \\ 0 & lk_f & 0 & -lk_f \\ -lk_f & 0 & lk_f & 0 \\ k_m & -k_m & k_m & -k_m \end{bmatrix} \begin{bmatrix} \omega_1^2 \\ \omega_2^2 \\ \omega_3^2 \\ \omega_4^2 \end{bmatrix} \tag{3}$$

where $k_f > 0$ and $k_m > 0$ are the thrust and moment coefficients of the rotors, respectively, and the distance between the axis of rotation and the center of mass is l. The net thrust is f and the moment about the ith body frame axis is given by M_i. Using this relationship, the system can be considered to have the control inputs pictured in Fig. 7.

Then, the translational dynamics are

$$m\ddot{\mathbf{x}} = f R\mathbf{e}_3 - mg\mathbf{e}_3 \tag{4}$$

where $m \in \mathbb{R}$ is the mass of the vehicle and $\mathbf{x} \in \mathbb{R}^3$ is the position of the robot in the world frame, $\mathcal{W}$ (see Ref. [28]). The rotation from the body frame, $\mathcal{B}$, to the world frame, $\mathcal{W}$, is given by $R \in \mathrm{SO}(3)$, g is the gravitational acceleration, and $\mathbf{e}_3$ is the third standard basis vector, $\mathbf{e}_3 = \begin{bmatrix} 0 & 0 & 1 \end{bmatrix}^{\mathrm{T}}$. The angular dynamics of the system are given by

$$J\dot{\Omega} = \mathbf{M} - \Omega \times J\Omega \tag{5}$$

where $J \in \mathbb{R}^{3\times3}$ is the inertia tensor aligned with $\mathcal{B}$, $\Omega \in \mathbb{R}^3$ is the angular velocity of the vehicle expressed in $\mathcal{B}$, and $\mathbf{M} = \begin{bmatrix} M_1 & M_2 & M_3 \end{bmatrix}^{\mathrm{T}}$ contains the control moments. Equations (4) and (5) are related through the orientation of the robot, namely

$$\dot{R} = R\hat{\Omega} \tag{6}$$

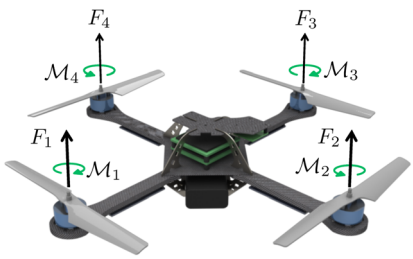

Fig. 6 A quadrotor has four rotating propellers. Each rotor generates a force, F_i, and a moment, $\mathcal{M}_i$. Adjacent rotors spin the opposite direction so that the moment resulting from drag is opposing and can be controlled by varying the speed of the pairs of rotors.

where $\hat{\cdot}: \mathbb{R}^3 \mapsto \mathfrak{so}(3)$ is the "hat" map and is defined such that if $\mathbf{a}, \mathbf{b} \in \mathbb{R}^3$, $\mathbf{a} \times \mathbf{b} = \hat{\mathbf{a}}\mathbf{b}$.

The Control Law. We implement the control law developed in Ref. [28], which guarantees exponential stability if the geodesic attitude error is less than 90 deg and exhibits almost global exponential attractiveness (the only exception is when the geodesic attitude error is 180 deg). Let the thrust be

$$f = (-k_x\mathbf{e}_x - k_v\mathbf{e}_v + mg\mathbf{e}_3 + m\ddot{\mathbf{x}}_d) \cdot R\mathbf{e}_3 \equiv \mathbf{f}_{\mathrm{des}} \cdot R\mathbf{e}_3 \tag{7}$$

where k_x and k_v are positive gains

$$\mathbf{e}_x = \mathbf{x} - \mathbf{x}_d \quad \text{and} \quad \mathbf{e}_v = \dot{\mathbf{x}} - \dot{\mathbf{x}}_d$$

are position and velocity errors, respectively, and $\ddot{\mathbf{x}}_d$ is the nominal acceleration. The commanded moments are given by

$$\mathbf{M} = -k_R\mathbf{e}_R - k_\Omega\mathbf{e}_\Omega + \Omega \times J\Omega - J\left(\hat{\Omega}R^{\mathrm{T}}R_c\Omega_c - R^{\mathrm{T}}R_c\dot{\Omega}_c\right) \tag{8}$$

where k_R and k_Ω are positive gains and

$$\mathbf{e}_R = \frac{1}{2}\left(R_c^{\mathrm{T}}R - R^{\mathrm{T}}R_c\right)^\vee \quad \text{and} \quad \mathbf{e}_\Omega = \Omega - R^{\mathrm{T}}R_c\Omega_c$$

are the angular position and rate errors with $\cdot^\vee : \mathfrak{so}(3) \mapsto \mathbb{R}^3$ being the opposite of the hat map. In this case, $\Omega_c \in \mathbb{R}^3$ is the "commanded" or nominal angular rate and R_c is the commanded attitude, which is given by

$$R_c = \begin{bmatrix} \mathbf{b}_{1_c}, & \mathbf{b}_{3_c} \times \mathbf{b}_{1_c}, & \mathbf{b}_{3_c} \end{bmatrix} \tag{9}$$

where

$$\mathbf{b}_{3_c} = \frac{-k_x\mathbf{e}_x - k_v\mathbf{e}_v - mg\mathbf{e}_3 + m\ddot{\mathbf{x}}_d}{\left\| -k_x\mathbf{e}_x - k_v\mathbf{e}_v - mg\mathbf{e}_3 + m\ddot{\mathbf{x}}_d \right\|} \tag{10}$$

and $\mathbf{b}_{1_c}$ is chosen such that $\mathbf{b}_{3_c} \times \mathbf{b}_{1_c}$ is well conditioned. In our case, $\mathbf{b}_{1_c}$ is defined by a combination of the planned trajectory and the desired force and will be explained further in the next section, Planning With Constraints.

Planning With Constraints

The system is underactuated since the thrust can only directly affect the translational acceleration in the $\mathbf{b}_3$ direction, and the moments can only directly affect the angular acceleration. Since we are interested in aggressive maneuvers in which the quadrotor can perch on vertical surfaces, it is important to ensure that we can plan trajectories that are not only dynamically feasible (considering the underactuation) but also physically realizable (considering actuator and sensor constraints). We will first explore the dynamic feasibility of a trajectory by presenting a planning method that, by design, can guarantee that a trajectory is dynamically feasible.

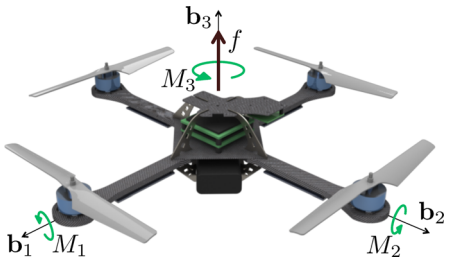

Fig. 7 The control inputs of a quadrotor can be considered to be a net force, f, and moments about each of the principal axes, M_i

Planning for Dynamic Feasibility. In this subsection, we will present results similar to Ref. [29], which facilitates the computation of trajectories for the underactuated quadrotor system. We propose the following set of variables called *flat outputs*, which will be used to show that the control inputs and state of the system can be expressed in terms of this subset of variables and their derivatives

$$\mathcal{Y} = \left[\mathbf{x}^{\mathrm{T}}, \psi\right] \tag{11}$$

where $\mathbf{x}$ is the position of the vehicle and ψ defines the yaw angle. In particular, these results will provide insight into how sufficiently smooth trajectories in the flat output space can be used to guarantee dynamic feasibility. This property of the system is called *differential flatness*, and has also been shown to be useful for planning trajectories for other underactuated systems [30,31].

First, observe from Eq. (4) that the nominal force can be determined from the acceleration of the trajectory, $\ddot{\mathbf{x}}$, since $\|R\mathbf{e}_3\| = 1$

$$f = m\|\ddot{\mathbf{x}} + g\mathbf{e}_3\| \tag{12}$$

and the orientation of the third body frame axis, $\mathbf{b}_3$ as in Fig. 7, is

$$R\mathbf{e}_3 = \mathbf{b}_3 = \frac{\ddot{\mathbf{x}} + g\mathbf{e}_3}{\|\ddot{\mathbf{x}} + g\mathbf{e}_3\|} \tag{13}$$

The rest of the rotation matrix, R, can be determined by defining a vector, $\mathbf{b}_1$ orthogonal to $\mathbf{b}_3$ using ψ and then using $\mathbf{b}_3 \times \mathbf{b}_1$ to determine $\mathbf{b}_2$. In Ref. [29], an intermediate vector was defined as $\mathbf{b}_c = \left[\cos\psi, \quad \sin\psi, \quad 0\right]$ so that $\mathbf{b}_2$ could be determined directly by

$$\mathbf{b}_2 = \frac{\mathbf{b}_3 \times \mathbf{b}_c}{\|\mathbf{b}_3 \times \mathbf{b}_c\|} \tag{14}$$

However, in our case, such an approach is dangerously close to the singularity that results when $\mathbf{b}_3$ is parallel to $\mathbf{b}_c$, which is likely to be the case when perching on a vertical surface since the thrust vector may be horizontal. To avoid this, we choose $\mathbf{b}_c$ such that the singularity is avoided by allowing $\mathbf{b}_c$ to be rotated (no more than $\pm\pi/2$) while remaining in the plane defined by $\left[\cos\psi, \quad \sin\psi, \quad 0\right] \times \mathbf{e}_3$. In practice, this means that we can define $\mathbf{b}_c$ as

$$\mathbf{b}_c = \begin{bmatrix} \cos\gamma\cos\psi \\ \cos\gamma\sin\psi \\ \sin\gamma \end{bmatrix}, \quad \gamma \in (-\pi, \pi) \tag{15}$$

where γ is chosen based on $\mathbf{b}_3$ (see Fig. 8). Then, $\mathbf{b}_2$ is given by Eq. (14),

$$\mathbf{b}_1 = \mathbf{b}_2 \times \mathbf{b}_3 \tag{16}$$

and

$$R = \left[\mathbf{b}_1, \quad \mathbf{b}_2, \quad \mathbf{b}_3\right] \tag{17}$$

The next derivative of Eq. (4) is given by

$$\begin{aligned} m\mathbf{x}^{(3)} &= f\dot{R}\mathbf{e}_3 + \dot{f}R\mathbf{e}_3 \\ &= fR\hat{\Omega}\mathbf{e}_3 + \dot{f}\mathbf{b}_3 \end{aligned} \tag{18}$$

and the scalar projection onto $\mathbf{b}_3$ reveals that

$$\dot{f} = \mathbf{b}_3 \cdot m\mathbf{x}^{(3)} \tag{19}$$

Next, we can determine the first two terms of Ω by solving Eq. (18) for $\hat{\Omega}\mathbf{e}_3$ and independently projecting onto $-\mathbf{e}_2$ and $\mathbf{e}_1$ (note that $R^{\mathrm{T}}\mathbf{b}_i = \mathbf{e}_i$ and, similarly, $\mathbf{e}_i^{\mathrm{T}}R^{\mathrm{T}} = \mathbf{b}_i^{\mathrm{T}}$)

$$\begin{bmatrix} \Omega_1 \\ \Omega_2 \end{bmatrix} = \frac{m}{f}\begin{bmatrix} -\mathbf{b}_2^{\mathrm{T}} \\ \mathbf{b}_1^{\mathrm{T}} \end{bmatrix}\mathbf{x}^{(3)} \tag{20}$$

The third term of Ω is constrained by $\dot{\psi}$. Consider

$$\Omega^{\mathcal{W}} = \begin{bmatrix} - \\ - \\ \dot{\psi} \end{bmatrix} = R\Omega \tag{21}$$

where $\Omega^{\mathcal{W}}$ is the angular velocity of the body expressed in the world coordinates. Then, Ω_3 can be determined using $\mathbf{e}_3^{\mathrm{T}}R\Omega$

$$\Omega_3 = \frac{\dot{\psi} - \mathbf{e}_3^{\mathrm{T}}(\mathbf{b}_1\Omega_1 + \mathbf{b}_2\Omega_2)}{\mathbf{e}_3^{\mathrm{T}}\mathbf{b}_3} \tag{22}$$

Now we have introduced a singularity that is, to the best of our knowledge, unavoidable in the full 3D case. Thus, any portion of the trajectory that passes through the singularity, we formulate as a vertical planar model, which results in a reduced-dimensioned flat space with $\Omega_3 = 0$ as a constant when expressed in 3D.

Another derivative of Eq. (4) provides

$$m\mathbf{x}^{(4)} = f\left(R\,\hat{\dot{\Omega}}\mathbf{e}_3 + R\hat{\Omega}\hat{\Omega}\mathbf{e}_3\right) + \dot{f}R\hat{\Omega}\mathbf{e}_3 + \ddot{f}\mathbf{b}_3 \tag{23}$$

and projecting onto $\mathbf{b}_3$

$$\ddot{f} = m\mathbf{b}_3^{\mathrm{T}}\mathbf{x}^{(4)} - f\mathbf{e}_3^{\mathrm{T}}\hat{\Omega}^2\mathbf{e}_3 \tag{24}$$

Similar to Eqs. (18) and (20), we can solve for the $\hat{\dot{\Omega}}\mathbf{e}_3$ term and use the scalar projections onto $\mathbf{e}_1$ and $-\mathbf{e}_2$ to determine the first two elements of $\dot{\Omega}$. The third element can then be determined and will require $\ddot{\psi}$. Having the angular acceleration, we can solve for the required moments.

Thus, the control inputs and the state of the robot can be expressed in terms of the *flat outputs* and their derivatives, which is a result from the *differential flatness* property [31]. In particular, we see that the fourth derivative of position and the second derivative of the yaw angle appear in the control inputs. Then, any trajectory that is sufficiently smooth in the flat outputs ($\mathbf{x}(t) \in \mathcal{C}^4$ and $\psi \in \mathcal{C}^2$) defines a trajectory which satisfies the dynamics of the system, and is therefore a dynamically feasible trajectory.

Actuator and Sensor Constraints. In addition to dynamic feasibility, we must also consider actuator and sensor constraints, especially when planning aggressive trajectories. While the trajectories are defined in the flat space, it is likely that the physical constraints are not defined directly in the flat space. Next, we will demonstrate how these constraints can be mapped to constraints

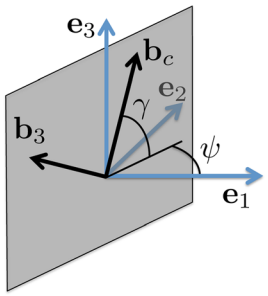

Fig. 8 We define the $\mathbf{b}_c$ vector based on ψ and $\mathbf{b}_3$ in order to determine $\mathbf{b}_2$ while avoiding the singularity when $\mathbf{e}_3 \cdot \mathbf{b}_3 = 0$

in the flat space, which enables their consideration when planning trajectories.

First, the net thrust is bounded by $f_{\max}$, which can be expressed as

$$m\|\ddot{\mathbf{x}} + g\mathbf{e}_3\| \leq f_{\max} \tag{25}$$

The gyros saturate at $\omega_{\max}$, which imposes a bound on the jerk expressed from Eq. (20) with a β_1 function as

$$\beta_1\left(\mathbf{x}^{(3)}, \ddot{\mathbf{x}}, \dot{\psi}\right) \leq \omega_{\max} \tag{26}$$

and the maximum moment about the ith axis is bounded by $M_{i_{\max}}$, requiring that

$$\beta_2\left(\mathbf{x}^{(4)}, \mathbf{x}^{(3)}, \ddot{\mathbf{x}}, \ddot{\psi}, \dot{\psi}\right) \leq M_{i_{\max}} \tag{27}$$

In practice, these constraints are coupled through Eq. (3). If the thrust is saturated, then all rotors are spinning at their maximum speed, and the moment inputs must be zero. Similarly, if a large moment is required, the thrust cannot simultaneously be zero. The thrust also cannot be zero because of the singularity in Eq. (13). For this reason, when planning, we further restrict certain constraints during portions of the trajectory that are expected to require large control inputs.

A Constrained Optimization Problem. The trajectories can be parametrized using an appropriate basis function (e.g., Legendre polynomials), $\mathbf{h}(t) \in \mathbb{R}^m$, and coefficients, $\mathbf{c}_i \in \mathbb{R}^m$, such that

$$\mathcal{Y}_i(t) = \mathbf{c}_i^{\mathrm{T}}\mathbf{h}(t) \text{ for } i = 1, \ldots, 4 \tag{28}$$

Next, an objective function is formulated to minimize the control inputs in the flat space [29]. Minimizing the integral of the square of the n_ith derivative of the ith flat output provides the cost function in Eq. (29).

$$\begin{aligned}\mathcal{J}_i &= \int_{t_0}^{t_f} \|\mathcal{Y}_i^{(n_i)}(t)\|^2 dt, \quad i = 1, \ldots, 4 \\ &= \mathbf{c}_i^{\mathrm{T}}\left[\int_{t_0}^{t_f} \mathbf{h}^{(n_i)}(t)\left[\mathbf{h}^{(n_i)}(t)\right]^{\mathrm{T}} dt\right]\mathbf{c}_i \\ &\equiv \mathbf{c}_i^{\mathrm{T}} H_i \mathbf{c}_i \end{aligned} \tag{29}$$

where, in our case, $n = \begin{bmatrix}4 & 4 & 4 & 2\end{bmatrix}$. Then, $H_i \in \mathbb{R}^{m\times m}$ is used to formulate the problem as a quadratic program (QP)

$$\begin{aligned} \text{minimize} \quad & C^{\mathrm{T}}\mathcal{H}C \\ \text{subject to} \quad & AC \leq B \\ & A_{\mathrm{eq}}C = B_{\mathrm{eq}} \end{aligned} \tag{30}$$

with

$$C = \begin{bmatrix}\mathbf{c}_1 \\ \vdots \\ \mathbf{c}_4\end{bmatrix}, \quad \mathcal{H} = \begin{bmatrix}H_1 & 0 & 0 \\ 0 & \ddots & 0 \\ 0 & 0 & H_4\end{bmatrix}$$

with the constraints discussed in the previous section, Actuator and Sensor Constraints, incorporated using a series of linear approximations in $A \in \mathbb{R}^{k\times 4m}$ and $B \in \mathbb{R}^k$ where k is the total number of linear constraints. The matrix $A_{\mathrm{eq}} \in \mathbb{R}^{p\times 4m}$ and vector $B_{\mathrm{eq}} \in \mathbb{R}^p$ can be used to impose p equality constraints. For example, we can use these to specify a velocity or acceleration constraint at a desired time.

The previous formulation is satisfactory for a single trajectory segment, but in practice, more than one segment is needed to maintain a high degree of freedom without resulting in computational errors. To keep the problem well conditioned, a desired trajectory is broken into segments with a maximum dt of 1 s. Then, the coefficients for each segment of a particular dimension can be stacked and incorporated into the QP. Finally, it is important to incorporate equality constraints between segments such that the ith dimension is $\mathcal{C}^{n_i}$.

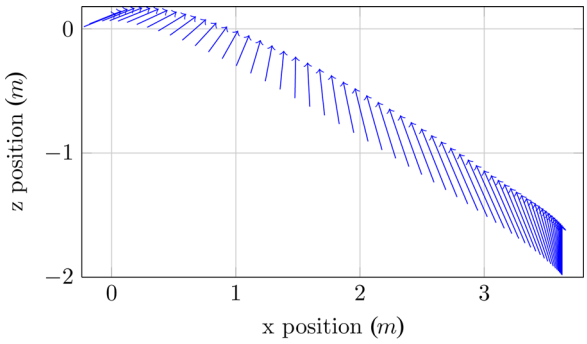

Fig. 9 A sample trajectory with vectors denoting the acceleration direction and magnitude. The quadrotor starts on the bottom right and perches on the left at an incline of 70 deg. The upper left corner is presented in a higher temporal resolution in Fig. 10.

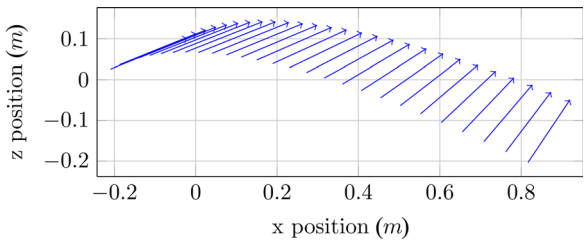

Fig. 10 The last 40 ms of a sample perching trajectory. The arrows denote the acceleration direction (i.e., the direction of $\mathbf{b}_3$) and magnitude. Notice that the direction of the vector does not change significantly toward the end of the trajectory where the acceleration is bounded during planning.

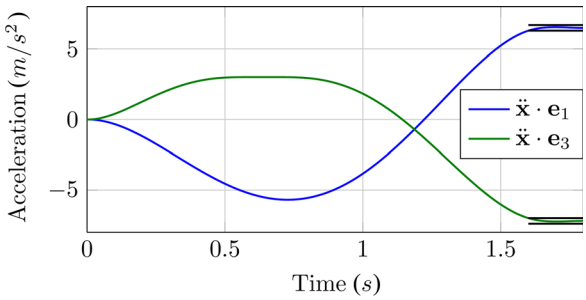

Fig. 11 A plot of the nominal acceleration for the trajectory in Fig. 9. Notice that during the last portion of the trajectory, the acceleration is bounded by the black lines, which dictates that the angular velocity will be nearly zero and that the robot will achieve the correct orientation before impact.

Boundary Conditions. Now, we will discuss the specific boundary conditions to enable successful perching using our quadrotor. The initial conditions can be chosen to match the current state. It is assumed that the position and orientation (orientation defined by a vector, $\mathbf{p}_3$, normal to the plane) of the perch plate are known. Thus, the position at impact is defined such that the quadrotor would be perched on the window. The desired normal impact velocity can be chosen from the landing envelope. A

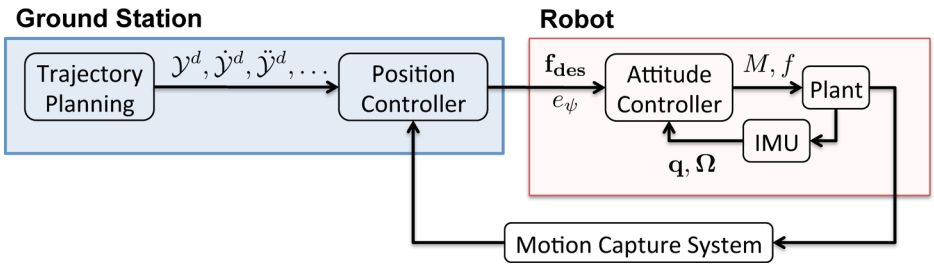

Fig. 12 The architecture of the system. The ground station handles the trajectory planning and passes the trajectories to the position controller, which receives feedback from the motion capture system. The position controller sends a desired force, $\mathbf{f_{des}}$, a ψ error, and the necessary feedforward inputs to the robot. Internally, the attitude controller runs at 1 kHz to update the commanded force and moments based on the position controller and the feedback from the IMU.

desired acceleration vector should be defined such that $\mathbf{b}_3$ (see Eq. (13)) is nearly aligned with $\mathbf{p}_3$ or slightly angled toward the plate so that the plane of the quadrotor is nearly parallel to the window and so that the highest pad makes contact first. In addition, the tangential velocity is desired to be slightly downward so that the highest pad is engaged as discussed in Fig. 4. These conditions should fall within the boundary given in Fig. 5.

From Ref. [19], we estimate that the time to change orientation will be a maximum of 0.4 s (assuming a change of $\pi/2$ radians). Thus, during the last portion of the trajectory, we specify an acceleration such that $\mathbf{b}_3$ is nearly constant and the magnitude of the acceleration places the thrust in the middle of its range to ensure that the robot has the moment control authority to rotate in case the orientation is lagging behind the desired. Note that it is important to consider gravity when using acceleration constraints to specify an attitude. For example, if we would like the $\mathbf{b}_3$ vector to be at an angle θ and the thrust to be $f_{\max}/2$, the acceleration must be expressed as

$$\ddot{\mathbf{x}}^d = \begin{bmatrix} \frac{f_{\max}}{2m}\sin(\theta) \\ 0 \\ \frac{f_{\max}}{2m}\cos(\theta) - g \end{bmatrix}$$

See Figs. 9 and 10 for a sample planar trajectory and acceleration vectors during the trajectory. See Fig. 11 for the components of acceleration. Notice that the acceleration is bounded toward the end of the trajectory to ensure that, if there is lag, the robot is still able to achieve the desired orientation before impact. Finally, to minimize unnecessary kinetic energy, we require that the angular rates are zero at impact.

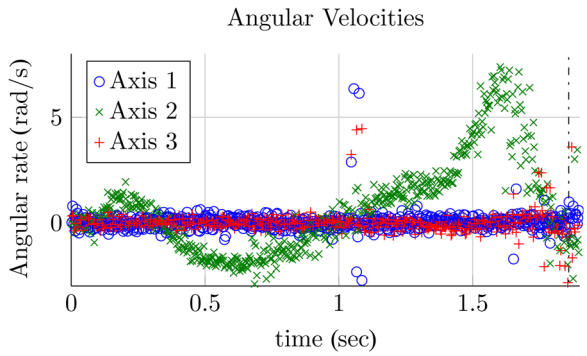

Fig. 13 The angular velocities for three different perching trials on a vertical surface as estimated by the motion capture system. The vertical dashed-dotted black line denotes the time of contact with the surface. As desired, the angular velocity is controlled to zero before impact.

Experimental Results

In this section, we present the experimental setup and the results of the perching trials. The experiments are conducted in the GRASP lab at the University of Pennsylvania (see Ref. [32]) using a Hummingbird quadrotor from Ascending Technologies,[2] and the QP is solved using Gurobi Optimizer 6.0[3] with the MATLAB® interface. A motion capture system is used for position feedback at 100 Hz. The setup is documented in Fig. 12. Successful perches on a vertical surface under various impact conditions are denoted by diamonds in Fig. 5. These demonstrate the effectiveness of the planning algorithm, controller, and gripper as the impact conditions fall within or near the boundary of the proposed landing envelope. The angular velocities for three vertical surface perches are overlaid in Fig. 13. In particular, we would like to highlight that at the time of impact, the angular velocity of the vehicle is nearly zero as desired. Further, the reader is encouraged to view an image sequence of a perching robot in Fig. 14 as well as the online multimedia material which is available on the ASME digital collection under the Supplemental Material tab.

In addition to perching on vertical surfaces, the robot is able to perch on various inclinations without the need for iterative experimental trials. For example, perches on surfaces at 30 deg, 50 deg, 70 deg, and 90 deg relative to the horizontal are presented in Fig. 15. Further, one of the motivations for the downward-facing gripper is that it can also be used to transport objects. For example, the robot could be used to retrieve a lost cell phone as pictured in Fig. 16.

Surface Effects. During these experiments, we noticed the impact of aerodynamic surface effects as the robot approached the perch plate. Even in quasi-static situations, surface effects are noticed [33]. Thus, this effect was not unexpected and will be explored further in future work.

Conclusion and Future Work

In this work, we presented a strategy for planning trajectories to enable quadrotors to perch on inclined surfaces while taking into account constraints due to dynamics, actuators, sensors, and the gripper. To show the effectiveness of the proposed methodology, we demonstrated perching on inclined (up to 90 deg) surfaces using a quadrotor equipped with a downward-facing dry-adhesive gripper. Future work will include perching on curved surfaces, batlike perching by hanging, and sensing failures during perching. We also intend to show how the presented methods can be adapted to quadrotors of various sizes. Another important future direction is the possibility to automate the gripper's detaching process using an onboard actuator, which will require balancing the need for compliance in a landing mechanism with the desire

[2] http://www.asctec.de
[3] http://www.gurobi.com

Fig. 14 A strobe of images from a perch sequence. The robot starts on the right hand side outside of the field of view, accelerates toward the target, and rotates in time to achieve a successful perch within the landing envelope of the gripper.

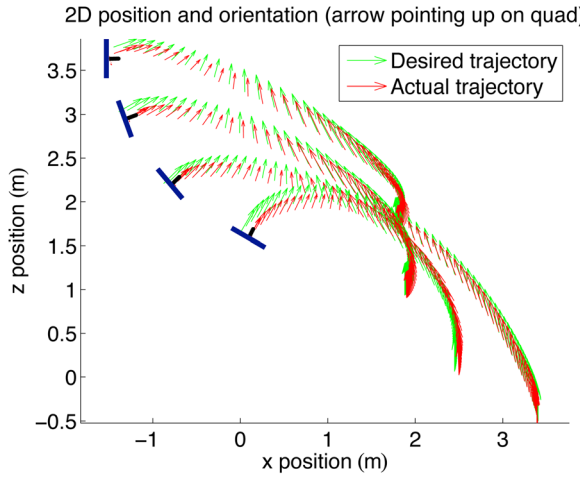

Fig. 15 Using the proposed planning method, the angle of the surface can be changed without the need for iterative experimental trials. The root of each arrow indicates the position of the robot, and the arrow indicates the direction of the thrust (i.e., the orientation of the robot).

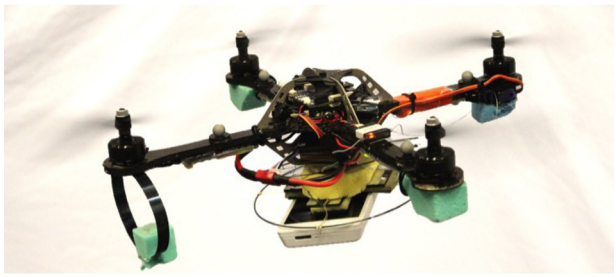

Fig. 16 The downward-facing gripper can also be used to carry payloads such as this cell phone

for a well-defined perching posture to simplify the return to free flight. Finally, we intend to move into real-world perching scenarios by exploring the impact of dusty surfaces on the gripper effectiveness, generalizing the gripper for other surfaces (e.g., brick, drywall, painted exterior metal, or marble) by using microspines or an appropriate amount of adhesive, and leveraging vision-based techniques to enable perching without a dependence on an external motion capture system.

Acknowledgment

The authors would like to thank Terry Kientz and Samer Nashed for their help in the design and mounting of the perch surface. We gratefully acknowledge the support by ARL Grant No. W911NF-08-2-0004, ONR Grant Nos. N00014-07-1-0829, N00014-14-1-0510, N00014-09-1-1051, and N00014-09-1-103, and NSF Grant Nos. IIP-1113830, IIS-1426840, and IIS-1138847.

References

[1] Mulgaonkar, Y., Whitzer, M., Kroninger, C. M., and Aaron, M., 2014, "Power and Weight Considerations in Small, Agile, Quadrotors," Proc. SPIE, **9083**, p. 90831Q.
[2] Lussier Desbiens, A., and Cutkosky, M. R., 2010, "Landing and Perching on Vertical Surfaces With Microspines for Small Unmanned Air Vehicles," J. Intell. Rob. Syst., **57**(1–4), pp. 313–327.
[3] Kovač, M., Germann, J., Hürzeler, C., Siegwart, R. Y., and Floreano, D., 2010, "A Perching Mechanism for Micro Aerial Vehicles," J. Micro Nano Mech., **5**(3–4), pp. 77–91.
[4] Lussier Desbiens, A., Asbeck, A. T., and Cutkosky, M. R., 2011, "Landing, Perching and Taking Off From Vertical Surfaces," Int. J. Rob. Res., **30**(3), pp. 355–370.
[5] Moore, J., and Tedrake, R., 2009, "Powerline Perching With a Fixed-Wing UAV," AIAA Infotech@Aerospace Conference, Seattle, WA, Apr. 6-9, AIAA Paper No. 2009–1959.
[6] Moore, J., Cory, R., and Tedrake, R., 2014, "Robust Post-Stall Perching With a Simple Fixed-Wing Glider Using LQR-Trees," Bioinspiration Biomimetics, **9**(2), p. 025013.
[7] Doyle, C. E., Bird, J. J., Isom, T. A., Johnson, C. J., Kallman, J. C., Simpson, J. A., King, R. J., Abbott, J. J., and Minor, M. A., 2011, "Avian-Inspired Passive Perching Mechanism for Robotic Rotorcraft," IEEE/RSJ International Conference on Intelligent Robots and Systems (IROS), San Francisco, CA, Sept. 25–30, pp. 4975–4980.
[8] Doyle, C. E., Bird, J. J., Isom, T. A., Kallman, J. C., Bareiss, D. F., Dunlop, D. J., King, R. J., Abbott, J. J., and Minor, M. A., 2013, "An Avian-Inspired Passive Mechanism for Quadrotor Perching," IEEE/ASME Trans. Mechatronics, **18**(2), pp. 506–517.
[9] Burroughs, M. L., Beauwen Freckleton, K., Abbott, J. J., and Minor, M. A., 2015, "A Sarrus-Based Passive Mechanism for Rotorcraft Perching," ASME J. Mech. Rob., **8**(1), p. 011010.
[10] Chi, W., Low, K. H., Hoon, K. H., and Tang, J., 2014, "An Optimized Perching Mechanism for Autonomous Perching With a Quadrotor," IEEE International Conference on Robotics & Automation (ICRA), Hong Kong, May 31–June 7, pp. 3109–3115.
[11] Hawkes, E. W., Christensen, D. L., Eason, E. V., Estrada, M. A., Heverly, M., Hilgemann, E., Jiang, H., Pope, M. T., Parness, A., and Cutkosky, M. R., 2013, "Dynamic Surface Grasping With Directional Adhesion," International Conference on Intelligent Robots and Systems (IROS), Tokyo, Nov. 3–7, pp. 5487–5493.
[12] Daler, L., Klaptocz, A., Briod, A., Sitti, M., and Floreano, D., 2013, "A Perching Mechanism for Flying Robots Using a Fibre-Based Adhesive," IEEE International Conference on Robotics and Automation (ICRA), Karlsruhe, Germany, May 6–10, pp. 4433–4438.
[13] Kalantari, A., Mahajan, K., Ruffatto, D., and Spenko, M., 2015, "Autonomous Perching and Take-Off on Vertical Walls for a Quadrotor Micro Air Vehicle," IEEE International Conference on Robotics and Automation (ICRA), Seattle, WA, May 26–30, pp. 4669–4674.
[14] Tsukagoshi, H., Watanabe, M., Hamada, T., Ashlih, D., and Iizuka, R., 2015, "Aerial Manipulator With Perching and Door-Opening Capability," 2015 IEEE International Conference on Robotics and Automation (ICRA), Seattle, WA, May 26–30, pp. 4663–4668.
[15] Jiang, H., Pope, M. T., Hawkes, E. W., Christensen, D. L., Estrada, M. A., Parlier, A., Tran, R., and Cutkosky, M. R., 2014, "Modeling the Dynamics of Perching With Opposed-Grip Mechanisms," IEEE International Conference on Robotics and Automation (ICRA), Hong Kong, May 31–June 7, pp. 3102–3108.
[16] Zhang, Z., Xie, P., and Ma, O., 2013, "Bio-Inspired Trajectory Generation for UAV Perching," IEEE/ASME International Conference on Advanced Intelligent Mechatronics (AIM), Wollongong, NSW, Australia, July 9–12, pp. 997–1002.
[17] Mellinger, D., Michael, N., and Kumar, V., 2010, "Trajectory Generation and Control for Precise Aggressive Maneuvers With Quadrotors," 12th International Symposium on Experimental Robotics (ISER), New Delhi, India, Dec. 18–21, pp. 361–373.
[18] Mellinger, D., Shomin, M., and Kumar, V., 2010, "Control of Quadrotors for Robust Perching and Landing," International Powered Lift Conference (IPLC), Philadelphia, PA, Oct. 5–7.
[19] Mellinger, D., Michael, N., and Kumar, V., 2012, "Trajectory Generation and Control for Precise Aggressive Maneuvers With Quadrotors," Int. J. Rob. Res., **31**(5), pp. 664–674.
[20] Mohta, K., Kumar, V., and Daniilidis, K., 2014, "Vision-Based Control of a Quadrotor for Perching on Lines," IEEE International Conference on Robotics and Automation (ICRA), Hong Kong, May 31–June 7, pp. 3130–3136.

[21] Thomas, J., Polin, J., Sreenath, K., and Kumar, V., 2013, "Avian-Inspired Grasping for Quadrotor Micro UAVs," ASME Paper No. DETC2013-13289.
[22] Thomas, J., Loianno, G., Pope, M., Hawkes, E. W., Estrada, M. A., Jiang, H., Cutkosky, M. R., and Kumar, V., 2015, "Planning and Control of Aggressive Maneuvers for Perching on Inclined and Vertical Surfaces," International Design Engineering Technical Conferences & Computers and Information in Engineering Conference (IDETC/CIE), Boston, MA, Aug. 2-5, ASME Paper No. DETC2015-47710.
[23] Hawkes, E. W., Jiang, H., and Cutkosky, M. R., 2015, "Three-Dimensional Dynamic Surface Grasping With Dry Adhesion," Int. J. Rob. Res., epub.
[24] Jiang, H., Hawkes, E. W., Arutyunov, V., Tims, J., Fuller, C., King, J. P., Seubert, C., Chang, H. L., Parness, A., and Cutkosky, M. R., "Scaling Controllable Adhesives to Grapple Floating Objects in Space," IEEE International Conference on Robotics and Automation (ICRA), Seattle, WA, May 26–30, pp. 2828–2835.
[25] Jiang, H., Pope, M. T., Estrada, M. A., Edwards, B., Cuson, M., Hawkes, E. W., and Cutkosky, M. R., 2015, "Perching Failure Detection and Recovery With Onboard Sensing," IEEE/RSJ International Conference on Intelligent Robots and Systems (IROS), Hamburg, Germany, Sept. 28–Oct. 2, pp. 1264-1270.
[26] Crandall, K. L., and Minor, M. A., 2015, "UAV Fall Detection From a Dynamic Perch Using Instantaneous Centers of Rotation and Inertial Sensing," IEEE International Conference on Robotics and Automation (ICRA), Seattle, WA, May 26–30, pp. 4675–4679.
[27] Estrada, M. A., Hawkes, E. W., Christensen, D. L., and Cutkosky, M. R., 2014, "Perching and Vertical Climbing: Design of a Multimodal Robot," IEEE International Conference on Robotics and Automation (ICRA), Hong Kong, May 31–June 7, pp. 4215–4221.
[28] Lee, T., Leoky, M., and McClamroch, N. H., 2010, "Geometric Tracking Control of a Quadrotor UAV on SE(3)," 49th IEEE Conference on Decision and Control (CDC), Atlanta, GA, Dec. 15–17, pp. 5420–5425.
[29] Mellinger, D., and Kumar, V., 2011, "Minimum Snap Trajectory Generation and Control for Quadrotors," IEEE International Conference on Robotics and Automation (ICRA), Shanghai, May 9–13, pp. 2520–2525.
[30] Fliess, M., Lévine, J., Martin, P., and Rouchon, P., 1995, "Flatness and Defect of Non-Linear Systems: Introductory Theory and Examples," Int. J. Control, **61**(6), Shanghai, May 9–13, pp. 1327–1361.
[31] Murray, R., Rathinam, M., and Sluis, W., 1995, "Differential Flatness of Mechanical Control Systems: A Catalog of Prototype Systems," ASME International Congress and Exposition, San Francisco, CA, Nov. 12–17.
[32] Michael, N., Mellinger, D., Lindsey, Q., and Kumar, V., 2010, "The GRASP Multiple Micro-UAV Testbed," IEEE Rob. Autom. Mag., **17**(3), pp. 56–65.
[33] Powers, C., Mellinger, D., Kushleyev, A., Kothmann, B., and Kumar, V., 2012, "Influence of Aerodynamics and Proximity Effects in Quadrotor Flight," 13th International Symposium on Experimental Robotics (ISER), Québec City, Canada, June 18–21, pp. 289–302.